# Exciton and Free Charge Dynamics of Methylammonium Lead Iodide Perovskites Are Different in the Tetragonal and Orthorhombic Phases

He Wang,[†,‡,§] Luisa Whittaker-Brooks,[⊥] and Graham R. Fleming[*,†,‡,§]

[†]Physical Biosciences Division, Lawrence Berkeley National Laboratory, Berkeley, California 94720, United States
[‡]Department of Chemistry, University of California, Berkeley, California 94720, United States
[§]Kavli Energy NanoSciences Institute, UC California, Berkeley, and the Lawrence Berkeley National Laboratory, Berkeley, California 94720, United States
[⊥]Department of Chemistry, University of Utah, Utah 84112, United States

ABSTRACT: The small exciton binding energy of perovskite suggests that the long-lived photoluminescence and slow recovery of the ground state bleaching of the tetragonal phase at room temperature results primarily from the decay of free charges rather than the decay of the initially created excitons. Here we demonstrate the ground state bleaching recovery of the orthorhombic phase of methylammonium lead iodide ($CH_3NH_3PbI_3$) is much faster than that of the tetragonal phase using temperature dependent transient absorption spectroscopy. The distribution in orientation of the methylammonium group which is disordered in the tetragonal phase and ordered in the orthorhombic phase results in smaller dielectric constant and larger exciton binding energy in the latter phase. We observe the recovery of the ground state bleaching in the orthorhombic phase to be comprised of decays of both excitons and free charges. Our findings suggest $CH_3NH_3PbI_3$ behaves like a nonexcitonic semiconductor in the tetragonal phase and an excitonic semiconductor in the orthorhombic phase.
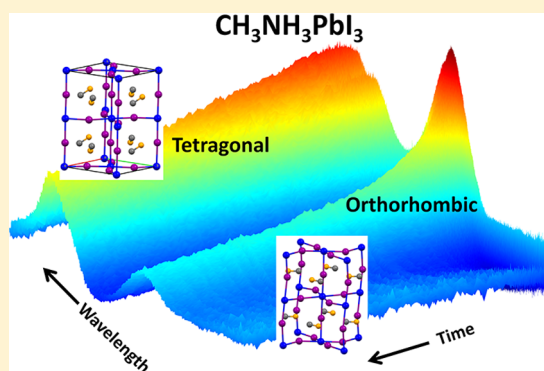
1. INTRODUCTION

The relationship between crystal structure and the strength of the exciton binding energy could provide a guide for rational design of optimized photovoltaic devices. It is therefore useful to explore this connection for the perovskite $CH_3NH_3PbI_3$ which has been extensively studied as a material for solar cell devices[1,2] because of a power conversion efficiency approaching 20%.[3−5] $CH_3NH_3PbI_3$ has two readily accessible crystal forms below room temperature: a tetragonal phase from 160 K to room temperature and an orthorhombic phase for temperatures below 160 K.[6,7] In addition to changes in the lattice constants as well as the tilting and rotation of the PbI_6 polyhedra between the two phases, the C−N bond of the methylammonium ion is disordered in the tetragonal phase and ordered parallel to the perovskite (001) plane in the orthorhombic phase.

The high power conversion efficiency of the room temperature $CH_3NH_3PbI_3$ tetragonal phase is attributed to high carrier mobility,[8−11] large dielectric constant,[6,12] low exciton binding energy,[12−14] likely well below kT at room temperature, and slow recombination of free charges.[11,15−19] Indeed the long-lived photoluminescence and slow recovery of the ground state bleaching is attributed to the decay of free charges rather than excitons.[15−23] In this work, we explore the role that crystal structure plays in these desirable properties for photovoltaic device formulation. Specifically, we examine the exciton and free charge dynamics of a $CH_3NH_3PbI_3$ thin film in both tetragonal and orthorhombic phases via temperature dependent transient absorption spectroscopy.

2. EXPERIMENTAL SECTION

2.1. Synthesis of Methylammonium Iodide (CH_3NH_3I) and Fabrication of $CH_3NH_3PbI_3$ Film. The CH_3NH_3I precursor was prepared by reacting 27 mL of methylamine (CH_3NH_2, 33% in absolute ethanol, Sigma-Aldrich) with 30 mL of hydroiodic acid (HI, 57% in water, Sigma-Aldrich) in a 250 mL round-bottom flask at 0 °C for 2 h under mild stirring. A white precipitate was collected using a rotary evaporator to carefully remove the solvents. To further purify the as-prepared CH_3NH_3I crystals, we redissolved the product in 100 mL of ethanol and reprecipitated the crystals by adding 100 mL of diethyl ether to the solution. This procedure was repeated three times. The final CH_3NH_3I crystals were collected and dried at 60 °C in a vacuum over for 24 h. The synthesized CH_3NH_3I (2.64 mol/L) and PbI_2 (0.88 mol/L, Alfa Aesar) were dissolved in anhydrous dimethylformamide (Sigma-Aldrich) and stirred overnight. The $CH_3NH_3PbI_3$ film was formed by spin coating

the solution at 2000 rpm for 2 min onto precleaned glass substrate in air. The film was then annealed at 135 °C for 15 min in air.

2.2. Powder X-ray Diffraction. Powder X-ray diffraction was collected with a Bruker D8 Advance diffractometer equipped with a Cu Kα source. The accelerating voltage and electrical current were 40 kV and 40 mA, respectively. The step size was 0.01° and the acquisition time was 40 min from 10° to 65° for 2θ. A glass slide was also scanned for the baseline correction.

2.3. Transient Absorption. Transient absorption spectra were collected via femtosecond pump probe spectroscopy. The pump beam was centered at 650 nm with full width at half-maximum of 31 nm. It was generated in a collinear optical parametric amplifier pumped by the 805 nm output of an amplified Ti:sapphire laser at repetition rate of 250 kHz. The pump beam, after compression by a pair of prisms, was around 45 fs duration. The pump energy at the sample was 10 nJ/pulse with a spot size diameter around 300 μm. The probe beam was a white light supercontinuum, created by the 805 nm output of an amplified Ti:sapphire laser passing through a 1 mm-thick sapphire plate. The probe beam was split into a signal beam, overlapping with the pump at a smaller size at the sample position, and a reference beam, not overlapping with the pump at the sample position. The reference beam was utilized to subtract intensity fluctuations. The shutters of the pump and probe were both mechanically controlled. The polarization between pump and probe beams was set at the magic angle (54.7°). The cross correlation between pump and probe was around 100 fs. The probe beam was spectrally resolved by a spectrometer and detected by a charge-coupled device camera. The spectrum at each temperature was averaged between 5 and 8 times. The sample was placed in the chamber of an Oxford Instruments liquid N_2 cryostat, with the continuous control and monitoring of the temperature between 77 and 295 K. Pump fluence dependent transient absorption spectra were detected by a silicon photodiode and a lock-in amplifier at 295 and 77 K around 760 nm. Different pump fluencies were obtained by neutral density filters.

3. RESULTS AND DISCUSSION

Parts a and b of Figure 1 display the crystal structures of the tetragonal and orthorhombic phases for $CH_3NH_3PbI_3$, respectively.[24] The tetragonal phase, where the methylammonium is disordered, exists from 160 K to room temperature.[24] The orthorhombic phase, where the methylammonium is ordered, exists below 160 K.[24] To investigate the structure and purity, we performed linear absorption and X-ray-diffracion (XRD) measurements. Parts c and d of Figure 1 display the linear absorption spectrum and XRD, respectively, of a $CH_3NH_3PbI_3$ film deposited on glass at room temperature. The linear absorption spectrum shows broad absorption with an absorption edge around 791 nm. As evidenced in the XRD trace, the peak at 11.4° which corresponds to reflection from planes in the PbI_2 structure is weak, indicating that the majority of the PbI_2 precursor has been converted to $CH_3NH_3PbI_3$. Likewise, the XRD trace presented in Figure 1d shows peaks at 14.0°, 28.3°, 31.2°, 43.0° which correspond to reflections associated with the (110), (220), (310), (330) crystallographic planes of the room temperature $CH_3NH_3PbI_3$ tetragonal phase.

Figure 2 shows the transient absorption spectra of $CH_3NH_3PbI_3$ acquired at 77, 100, 130, 160, 190, 220, 250, and 295 K (room temperature), with excitation at 650 nm,
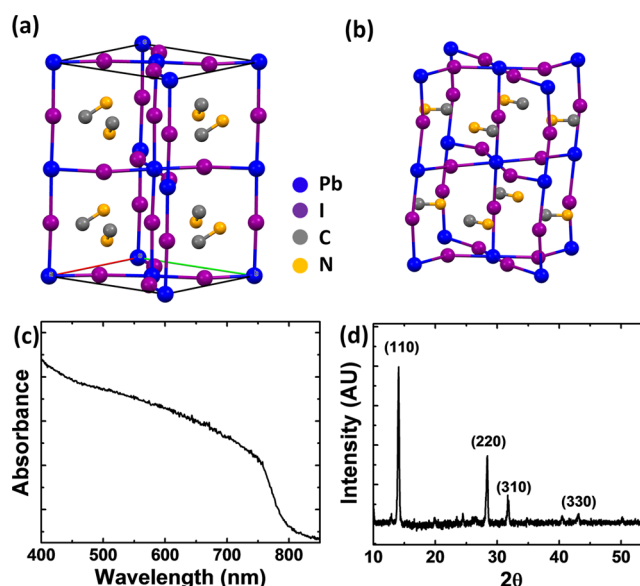

Figure 1. (a) Tetragonal and (b) orthorhombic phases of $CH_3NH_3PbI_3$. Cif files are from ref 24. (c) Linear absorption and (d) X-ray diffraction of $CH_3NH_3PbI_3$ at room temperature.

probe at 685−800 nm, and pump−probe decay time from −0.6 to +800 ps. The negative (blue) features correspond to ground state bleaching (GSB) and stimulated emission (SE). The peaks of the negative signals are labeled by dashed white lines for clarity purposes. The negative signal at room temperature appears around 765 nm, consistent with previous reports of $CH_3NH_3PbI_3$ transient absorption spectroscopy.[15,17,19,20] The positive features correspond to excited state absorption. As observed in Figure 2, one negative peak exists at all temperatures except 160 K. Right at 160 K, we observe two negative peaks, suggesting that both tetragonal and orthorhombic phases coexist at this temperature.

As shown by the dashed white lines in Figure 2, the negative feature is blue shifts with temperature for both tetragonal and orthorhombic phases. Figure 3 displays the energy of this transition as a function of temperature. The transition energy shows a positive linear trend with temperature for both phases. Since the transition around 760 nm is from the band edge GSB and SE, the positive trend originates from the positive thermal expansion coefficient of the band gap, dE_g/dT. A linear fit gives dE_g/dT to be 0.25 meV/K for the tetragonal phase and 0.28 meV/K for the orthorhombic phase. These values are similar to previously reported values of dE_g/dT for a lead composite.[25] The energy associated with the band edge transition of the orthorhombic phase is larger than that of the tetragonal phase. Our observation is consistent with previous reports showing the calculated and experimental band gap of the orthorhombic phase larger than that of the tetragonal phase.[7,26−29]

As shown in Figure 2, the decay rates of the negative signal in the two phases are significantly different. Consistent with previous reports,[15−23] we observe a long-lived negative signal for the tetragonal phase from 190 K to room temperature with a center wavelength around 765−780 nm. Surprisingly, however, the major portion of the negative signal of the orthorhombic phase from 77 to 130 K with a center wavelength around 738−748 nm is short-lived. A slower component also is evident. Our data do not indicate any definitive trend in the time scale of this component with temperature. At 160 K,
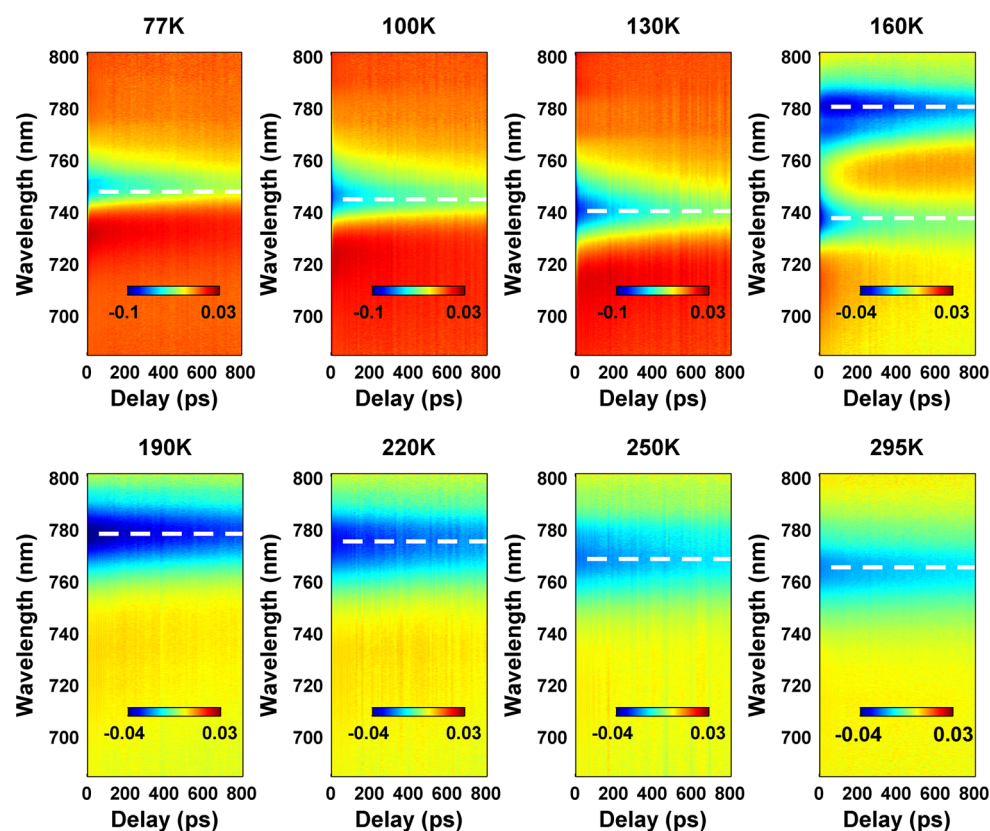
Figure 2. ΔOD maps as a function of probe wavelength (685−800 nm) and pump−probe delay (−0.6 to +800 ps) with excitation at 650 nm for various tempeatures. The negative feature associated with ground state bleaching and stimulated emission is labeled by a dashed white line in each figure.
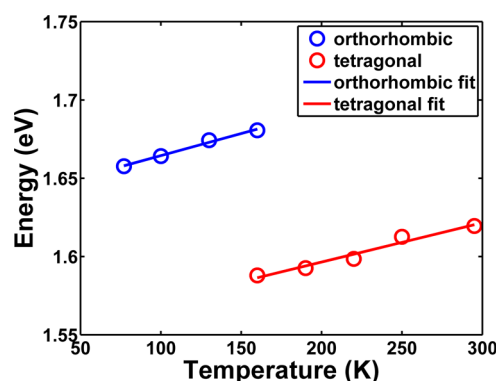
Figure 3. Energy associated with ground state bleaching and stimulated emission as a function of temperature for $CH_3NH_3PbI_3$ in the orthorhombic (blue circles) and tetragonal (red circles) phases. These energy values are extracted from the transient absorption spectra presented in Figure 2. The linear fits are shown in solid blue line for the orthorhombic phase and red line for the tetragonal phase.

signals having both long and short lifetimes are observed, due to the coexistence of the two structural phases.

Figure 4 displays representative time traces and fits probing at the center of negative feature for the orthorhombic phase, the coexistence regime, and the tetragonal phase at 77, 160, and 250 K, respectively. As depicted in Figure 4, the signal has two decay rates at low temperatures. For the tetragonal phase at 250 K, a biexponential fit gives a decay time of 48 ± 20 ps (6 ± 6%) and decay time of 1.9 ± 0.4 ns (94 ± 6%). Recently, Vardeny and co-workers utilized pulses of 0.8 eV (1550 nm) to probe

the excited state absorption of $CH_3NH_3PbI_3$.[30] The short-lived excited state absorption signals at 1550 nm relative to the long-lived ground state bleaching signals suggest the existence of excitons and the lifetime of excitons in $CH_3NH_3PbI_3$ to be shorter than that of free charges.[30] Since typically the lifetime of the free charges is orders of magnitude larger than that of exciton, we attribute the short component to exciton decay and the slow component to free charge decay due to electron−hole recombination. The slow dynamic is the dominant process, indicating that the majority of the excitons created in the tetragonal phase can easily separate into free electrons and holes. Such a result is not surprising given that the dielectric constant of $CH_3NH_3PbI_3$ in the tetragonal phase is large compared to most inorganic and organic materials.[6,12,31] The real part of the static dielectric constant of the tetragonal phase is 60−70 at room temperature[6,12] and 135 at 160 K.[6] Since the exciton binding energy is inversely proportional to the dielectric constant, the exciton binding energy of $CH_3NH_3PbI_3$ in the tetragonal phase has been predicted to be as small as 0.7 meV[14] to 2 meV.[12] For comparison, the dielectric constant and exciton binding energy of silicon are 11.7 and 15 meV, respectively,[12] while the dielectric constant and exciton binding energy of organic semiconductors range from 2−4 and around 0.3 eV, respectively.[31] At temperatures above 160 K, the short-lived component of the tetragonal phase has a weight of 0−10%. This suggests that the exciton binding energy of the tetragonal phase is small enough to enable efficient separation of free charges.

For the orthorhombic phase at 77 K, a biexponential fit gives decay times of 3.0 ± 1.5 ps (55 ± 2%) and of 0.9 ± 0.1 ns (45
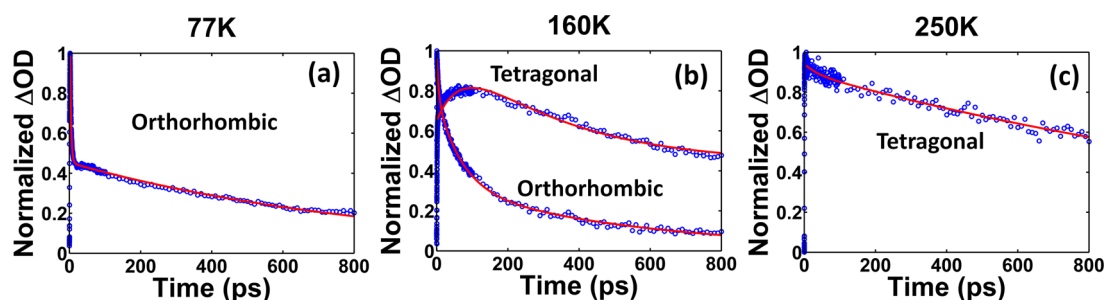
Figure 4. Normalized transient absorption signals at (a) 77 K with probe wavelength of 748 nm, (b) 160 K with probe wavelengths of 738 and 781 nm, and (c) 250 K with probe wavelength of 769 nm. The blue circles represent the experimental data. The red solid line represents biexponential fits at T = 77 and 250 K. At 160 K, the red solid line represents the three exponential decay component fit for the orthorhombic phase decay and the sum of biexponential decays and a single exponential rise for the tetragonal phase.
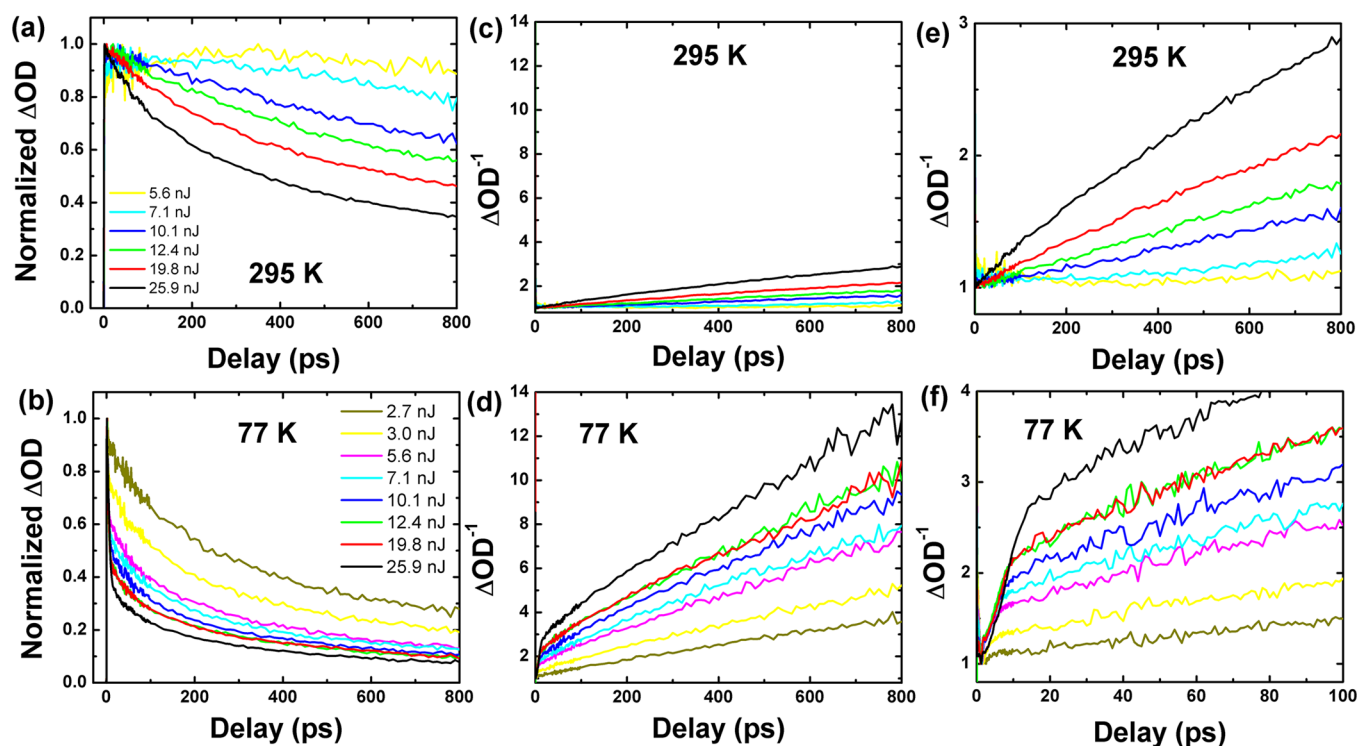
Figure 5. Normalized transient absorption signals at (a) room temperature 295 K and (b) 77 K at different pump intensities. (c) Reciprocal of kinetic traces shown in part a. (d) Reciprocal of kinetic traces shown in part b. The axes of parts c and d are the same for easy comparison. (e) Magnification of part c along the ΔOD^{-1} axis. The linearity suggests electron–hole recombination at room temperature. (f) Magnification of part d along the time axis to show the initial decay.

± 2%). The weight of the rapid decay (exciton decay) for the orthorhombic phase is much larger than that of the tetragonal phase. Hirasawa and co-workers estimated an exciton binding energy of 37 meV for the orthorhombic phase via mangetoasorption spectroscopy at 4.2 K.[32] Onoda-Yamamuro and co-workers compared the dielectric constant of both the tetragonal and orthorhombic phases.[6] The real part of the dielectric constant of $CH_3NH_3PbI_3$ in the orthorhombic phase (35 below 150 K) is much smaller than that of the tetragonal phase (135 at 160 K).[6] This arises from the permanent dipole of the methylammonium which is predominantly disordered in the tetragonal phase and ordered in the orthorhombic phase.[6] Given that exciton binding energy is inversely proportional to the dielectric constant, the exciton binding energy of the orthorhombic phase is expected to be larger than that of the tetragonal phase. In turn, this gives a larger contribution of excitons to the dynamics of the orthorhombic phase. Since the

real part of the dielectric constant of the orthorhombic phase is not sensitive to temperature,[6] temperature has little effect on the exciton binding energy, and primarily provides thermal energy for exciton dissociation. As expected, we observe the weight of the exciton to progressively decrease from 55 ± 2% at 77 K to 41 ± 2% at 100 K and 33 ± 1% at 130 K.

Another feature of the time-resolved data is the slow rising signal for the tetragonal phase at 160 K. This slow rise is only observed for the tetragonal phase at the temperature where the two phases coexist. Therefore, we suggest the slow rise signal is associated with energy/charge transfer from the orthorhombic phase to the tetragonal phase. We fit the bleach dynamics of the orthorhombic phase to three exponential components. Besides exciton and free charge decays, we observe a third exponential decay component with lifetime of 66 ± 13 ps. In order to verify the existence of energy/charge transfer from the orthorhombic phase to the tetragonal phase, we added an exponential rise to

our fit for tetragonal phase at 160 K. We find a rise time of 66 ± 13 ps to be able to successfully fit the rising signal, as shown in Figure 4b. The amplitude of the 66 ± 13 ps component in the orthorhombic phase is 0.43 ± 0.02, within error the same as the amplitude of the rise for the tetragonal phase, 0.38 ± 0.06, consistent with the existence of energy/charge transfer from the orthorhombic to the tetragonal phase. Such transfer indicates that these two phases are well mixed at the phase transition temperature.

The optical density of $CH_3NH_3PbI_3$ changes slightly with temperature.[13] We carried out fluence dependent transient absorption spectroscopy to study whether the optical density variation between the two phases is the main contribution to the variation in the decay rate. Parts a and b of Figure 5 display the normalized kinetic traces under different pump fluences at room temperature (tetragonal phase) and 77 K (orthorhombic phase), respectively. Within the range of pump fluences we tested, the decay in the orthorhombic phase is obviously faster than that in the tetragonal phase, suggesting that the significant variation in the decay rate between the two phases does not mainly originate from the optical density change.

Because of the linear relationship between normalized ΔOD^{-1} and time under different pump fluences at room temperature, Kamat and co-workers concluded the signal decay originates from the electron−hole recombination.[17] Parts c and d of Figure 5 display normalized ΔOD^{-1} as a function of time at room temperature and 77 K, respectively. For comparison, the data was plotted on the same scale. A magnification of Figure 5c is shown in Figure 5e. Consistent with Kamat's observation, we observed a linear relationship between ΔOD^{-1} and time. The comparison between parts c and d of Figure 5 in the hundreds of picoseconds to nanosecond range shows the larger slope in the orthorhombic phase than that in the tetragonal phase. Furthermore, the decay of the orthorhombic phase in the first few ps is much faster than that at longer times, as magnified in Figure 5f, suggesting differing origins of the decay in the ps and ns regions. Given that the excited state absorption signals at 1550 nm associated with exciton is short-lived,[30] we suspect the faster decay in the orthorhombic phase to mainly originate from exciton−exciton annihilation and the slower decay in the tetragonal phase to originate from electron−hole recombination. A quantitative analysis of fluence dependent transient absorption spectra between two different phases is under study and will be presented separately.

4. CONCLUSIONS

In summary, we demonstrate that the exciton and free charge dynamics of the tetragonal and orthorhombic phases are significantly different. The tetragonal phase is comprised primarily of free charges and the orthorhombic phase is comprised of both free charges and excitons. The difference in the fraction of excitons between two phases arises from the discontinuity of dielectric constant, which ultimately affects the exciton binding energy. The small exciton binding energy for the tetragonal phase resulting in rapid and efficient electron−hole separation makes the tetragonal phase less demanding of charge separation layer during device fabrication. We find that energy or charge can be transferred from the orthorhombic phase to the tetragonal phase. Our results suggest that orientational disorder can be a useful design motif to assist facile separation of electrons and holes in perovskite and related solar cells.

■ AUTHOR INFORMATION

Corresponding Author
*(G.R.F.) E-mail: fleming@cchem.berkeley.edu.

Notes
The authors declare no competing financial interest.

■ REFERENCES

(1) Green, M. A.; Ho-Baillie, A.; Snaith, H. J. The Emergence of Perovskite Solar Cells. *Nat. Photonics* **2014**, *8*, 506−514.

(2) Luo, S.; Daoud, W. A. Recent Progress in Organic-Inorganic Halide Perovskite Solar Cells: Mechanisms and Material Design. *J. Mater. Chem. A* **2015**, *3*, 8992−9010.

(3) Zhou, H.; Chen, Q.; Li, G.; Luo, S.; Song, T.-b.; Duan, H.-S.; Hong, Z.; You, J.; Liu, Y.; Yang, Y. Interface Engineering of Highly Efficient Perovskite Solar Cells. *Science* **2014**, *345*, 542−546.

(4) Nie, W.; Tsai, H.; Asadpour, R.; Blancon, J.-C.; Neukirch, A. J.; Gupta, G.; Crochet, J. J.; Chhowalla, M.; Tretiak, S.; Alam, M. A.; et al. High-Efficiency Solution-Processed Perovskite Solar Cells with Millimeter-Scale Grains. *Science* **2015**, *347*, 522−525.

(5) Green, M. A.; Emery, K.; Hishikawa, Y.; Warta, W.; Dunlop, E. D. Solar Cell Efficiency Tables (Version 45). *Prog. Photovoltaics* **2015**, *23*, 1−9.

(6) Onoda-Yamamuro, N.; Matsuo, T.; Suga, H. Dielectric Study of $CH_3NH_3PbX_3$ (X = Cl, Br, I). *J. Phys. Chem. Solids* **1992**, *53*, 935−939.

(7) Baikie, T.; Fang, Y.; Kadro, J. M.; Schreyer, M.; Wei, F.; Mhaisalkar, S. G.; Graetzel, M.; White, T. J. Synthesis and Crystal Chemistry of the Hybrid Perovskite (CH_3NH_3)PbI_3 for Solid-State Sensitised Solar Cell Applications. *J. Mater. Chem. A* **2013**, *1*, 5628−5641.

(8) Oga, H.; Saeki, A.; Ogomi, Y.; Hayase, S.; Seki, S. Improved Understanding of the Electronic and Energetic Landscapes of Perovskite Solar Cells: High Local Charge Carrier Mobility, Reduced Recombination, and Extremely Shallow Traps. *J. Am. Chem. Soc.* **2014**, *136*, 13818−13825.

(9) Wehrenfennig, C.; Eperon, G. E.; Johnston, M. B.; Snaith, H. J.; Herz, L. M. High Charge Carrier Mobilities and Lifetimes in Organolead Trihalide Perovskites. *Adv. Mater.* **2014**, *26*, 1584−1589.

(10) Wehrenfennig, C.; Liu, M.; Snaith, H. J.; Johnston, M. B.; Herz, L. M. Charge-Carrier Dynamics in Vapour-Deposited Films of the Organolead Halide Perovskite $CH_3NH_3PbI_{3-x}Cl_x$. *Energy Environ. Sci.* **2014**, *7*, 2269−2275.

(11) Ponseca, C. S.; Savenije, T. J.; Abdellah, M.; Zheng, K.; Yartsev, A.; Pascher, T.; Harlang, T.; Chabera, P.; Pullerits, T.; Stepanov, A.; et al. Organometal Halide Perovskite Solar Cell Materials Rationalized: Ultrafast Charge Generation, High and Microsecond-Long Balanced Mobilities, and Slow Recombination. *J. Am. Chem. Soc.* **2014**, *136*, 5189−5192.

(12) Lin, Q.; Armin, A.; Nagiri, R. C. R.; Burn, P. L.; Meredith, P. Electro-Optics of Perovskite Solar Cells. *Nat. Photonics* **2015**, *9*, 106−112.

(13) D'Innocenzo, V.; Grancini, G.; Alcocer, M. J. P.; Kandada, A. R. S.; Stranks, S. D.; Lee, M. M.; Lanzani, G.; Snaith, H. J.; Petrozza, A. Excitons Versus Free Charges in Organo-Lead Tri-Halide Perovskites. *Nat. Commun.* **2014**, *5*, 3586.

(14) Frost, J. M.; Butler, K. T.; Brivio, F.; Hendon, C. H.; van Schilfgaarde, M.; Walsh, A. Atomistic Origins of High-Performance in Hybrid Halide Perovskite Solar Cells. *Nano Lett.* **2014**, *14*, 2584−2590.

(15) Stranks, S. D.; Eperon, G. E.; Grancini, G.; Menelaou, C.; Alcocer, M. J. P.; Leijtens, T.; Herz, L. M.; Petrozza, A.; Snaith, H. J. Electron-Hole Diffusion Lengths Exceeding 1 Micrometer in an Organometal Trihalide Perovskite Absorber. *Science* **2013**, *342*, 341−344.

(16) Sum, T. C.; Mathews, N. Advancements in Perovskite Solar Cells: Photophysics Behind the Photovoltaics. *Energy Environ. Sci.* **2014**, *7*, 2518−2534.

(17) Manser, J. S.; Kamat, P. V. Band Filling with Free Charge Carriers in Organometal Halide Perovskites. *Nat. Photonics* **2014**, *8*, 737−743.

(18) Stamplecoskie, K. G.; Manser, J. S.; Kamat, P. V. Dual Nature of the Excited State in Organic-Inorganic Lead Halide Perovskites. *Energy Environ. Sci.* **2015**, *8*, 208−215.

(19) Xing, G.; Mathews, N.; Sun, S.; Lim, S. S.; Lam, Y. M.; Gratzel, M.; Mhaisalkar, S.; Sum, T. C. Long-Range Balanced Electron- and Hole-Transport Lengths in Organic-Inorganic $CH_3NH_3PbI_3$. *Science* **2013**, *342*, 344−347.

(20) Wang, L.; McCleese, C.; Kovalsky, A.; Zhao, Y.; Burda, C. Femtosecond Time-Resolved Transient Absorption Spectroscopy of $CH_3NH_3PbI_3$ Perovskite Films: Evidence for Passivation Effect of PbI_2. *J. Am. Chem. Soc.* **2014**, *136*, 12205−12208.

(21) Deschler, F.; Price, M.; Pathak, S.; Klintberg, L. E.; Jarausch, D.-D.; Higler, R.; Huttner, S.; Leijtens, T.; Stranks, S. D.; Snaith, H. J.; et al. High Photoluminescence Efficiency and Optically Pumped Lasing in Solution-Processed Mixed Halide Perovskite Semiconductors. *J. Phys. Chem. Lett.* **2014**, *5*, 1421−1426.

(22) Kim, H.-S.; Lee, C.-R.; Im, J.-H.; Lee, K.-B.; Moehl, T.; Marchioro, A.; Moon, S.-J.; Humphry-Baker, R.; Yum, J.-H.; Moser, J. E.; et al. Lead Iodide Perovskite Sensitized All-Solid-State Submicron Thin Film Mesoscopic Solar Cell with Efficiency Exceeding 9%. *Sci. Rep.* **2012**, *2*, 591.

(23) Marchioro, A.; Teuscher, J.; Friedrich, D.; Kunst, M.; van de Krol, R.; Moehl, T.; Gratzel, M.; Moser, J.-E. Unravelling the Mechanism of Photoinduced Charge Transfer Processes in Lead Iodide Perovskite Solar Cells. *Nat. Photonics* **2014**, *8*, 250−255.

(24) Feng, J.; Xiao, B. Crystal Structures, Optical Properties, and Effective Mass Tensors of $CH_3NH_3PbX_3$ (X = I and Br) Phases Predicted from HSE06. *J. Phys. Chem. Lett.* **2014**, *5*, 1278−1282.

(25) Karczewski, G.; Klimkiewicz, M.; Glass, I.; Szczerbakow, A.; Behrendt, R. Temperature and Composition Dependence of the Energy Band Gap of $Pb_{1-x}Mn_xS$ Solid Solution. *Appl. Phys. A: Solids Surf.* **1982**, *29*, 49−52.

(26) Geng, W.; Zhang, L.; Zhang, Y.-N.; Lau, W.-M.; Liu, L.-M. First-Principles Study of Lead Iodide Perovskite Tetragonal and Orthorhombic Phases for Photovoltaics. *J. Phys. Chem. C* **2014**, *118*, 19565−19571.

(27) Zhu, X.; Su, H.; Marcus, R. A.; Michel-Beyerle, M. E. Computed and Experimental Absorption Spectra of the Perovskite $CH_3NH_3PbI_3$. *J. Phys. Chem. Lett.* **2014**, *5*, 3061−3065.

(28) Xing, G.; Mathews, N.; Lim, S. S.; Yantara, N.; Liu, X.; Sabba, D.; Gratzel, M.; Mhaisalkar, S.; Sum, T. C. Low-Temperature Solution-Processed Wavelength-Tunable Perovskites for Lasing. *Nat. Mater.* **2014**, *13*, 476−480.

(29) Wehrenfennig, C.; Liu, M.; Snaith, H. J.; Johnston, M. B.; Herz, L. M. Charge Carrier Recombination Channels in the Low-Temperature Phase of Organic-Inorganic Lead Halide Perovskite Thin Films. *APL Mater.* **2014**, *2*, 081513.

(30) Sheng, C.; Zhang, C.; Zhai, Y.; Mielczarek, K.; Wang, W.; Ma, W.; Zakhidov, A.; Vardeny, Z. V. Exciton versus Free Carrier Photogeneration in Organometal Trihalide Perovskites Probed by Broadband Ultrafast Polarization Memory Dynamics. *Phys. Rev. Lett.* **2015**, *114*, 116601.

(31) Torabi, S.; Jahani, F.; Van Severen, I.; Kanimozhi, C.; Patil, S.; Havenith, R. W. A.; Chiechi, R. C.; Lutsen, L.; Vanderzande, D. J. M.; Cleij, T. J.; et al. Strategy for Enhancing the Dielectric Constant of Organic Semiconductors Without Sacrificing Charge Carrier Mobility and Solubility. *Adv. Funct. Mater.* **2015**, *25*, 150−157.

(32) Hirasawa, M.; Ishihara, T.; Goto, T.; Uchida, K.; Miura, N. Magnetoabsorption of the Lowest Exciton in Perovskite-Type Compound $(CH_3NH_3)PbI_3$. *Phys. B* **1994**, *201*, 427−430.